Chronic enrichment of hepatic ER-mitochondria contact sites leads to calcium dependent mitochondrial dysfunction in obesity

Citation

Published Version

Permanent link

http://nrs.harvard.edu/urn-3:HUL.InstRepos:17295575

Terms of Use

Share Your Story

Accessibility

Chronic enrichment of hepatic ER-mitochondria contact sites leads to calcium dependent mitochondrial dysfunction in obesity

Ana Paula Arruda[1,2], **Benedicte Mengel Pers**[1,2], **Güneş Parlakgül**[1], **Ekin Güney**[1], **Karen Inouye**[1], and **Gökhan S. Hotamisligil**[1,*]

[1]Department of Genetics and Complex Diseases and Sabri Ülker Center for Genetic and Metabolic Research, Harvard School of Public Health, Boston, MA 02115

Abstract

Proper function of the endoplasmic reticulum (ER) and mitochondria is critical for cellular homeostasis, and dysfunction at either site has been linked to pathophysiological states including metabolic diseases. Although ER and mitochondria play distinct cellular roles, these organelles also form physical interactions at sites defined as mitochondria associated ER-membranes (MAMs), which are essential for Ca^{2+}, lipid and metabolite exchange. Here we show that in the liver, obesity leads to a significant reorganization of MAMs resulting in mitochondrial Ca^{2+} overload, compromised mitochondrial oxidative capacity and augmented oxidative stress. Experimental induction of ER-mitochondria interactions results in oxidative stress and impaired metabolic homeostasis, while down-regulation of PACS-2 or IP3R1, proteins important for ER-mitochondria tethering and calcium transport respectively, improves mitochondrial oxidative capacity and insulin sensitivity in obese animals. These findings establish excessive ER-mitochondrial coupling as an essential component of organelle dysfunction in obesity, which may contribute to the development of metabolic pathologies such as insulin resistance.

Introduction

Obese individuals are at increased risk for developing insulin resistance and are predisposed to many pathologies including diabetes and cardiovascular disease[1,2]. Although the molecular mechanisms that underlie these associations are not completely defined, dysfunction of cellular organelles such as endoplasmic reticulum (ER) and mitochondria has emerged as a key event in the alterations that follow nutrient overload[3,4]. For example, in the liver of obese animals the ER membrane lipid composition is altered[5]; its capacity to retain Ca^{2+} is impaired[5], and ER protein degradation machinery is suppressed[6]. As a consequence, the unfolded protein response (UPR) is activated, impacting a variety of

inflammatory, metabolic, and stress-signaling networks directly involved in metabolic diseases[3,7,8]. ER stress is also detected in obese humans[9,10], and interventions that improve ER function have been shown to restore glucose homeostasis in mouse models as well as in obese and diabetic patients[11–13].

It has also been established in humans and mouse models that obesity results in mitochondrial dysfunction in skeletal muscle and adipose tissue, featuring altered oxidative function, ultrastructure abnormalities, and increased oxidative stress[14–20]. In the liver, although there is variability between studies, obesity is associated with altered oxidative capacity and excessive oxidative stress both in humans and mice[21–24]. However, the degree of mitochondrial defects, the underlying molecular mechanisms, and the consequences for systemic metabolic control are not well established[4,14,17–20].

Based on the distinct roles that ER and mitochondria play in the cell, the metabolic impacts of ER and mitochondrial dysfunction have largely been viewed and studied independently. However, these organelles physically and functionally interact and are able to regulate each other's function[25]. The sites of physical communication between ER and mitochondria, defined as mitochondria associated ER membranes (MAMs), are conserved structures found across eukaryotic phyla, and are key determinants of cell survival and death through the transfer of Ca^{2+} and other metabolites[25]. In addition, this subdomain of the ER is responsible for the biosynthesis of two abundant phospholipids, phosphatidylcholine and phosphatidylethanolamine[25]. Recently it was also shown that MAMs are important for autophagy by regulating autophagosome formation[26] and for mitochondrial dynamics by marking sites of mitochondrial fission[27]. Thus the function or dysfunction of one organelle can profoundly affect the other, but the relevance of this interaction to obesity-related cellular dysfunction and metabolic homeostasis has not been studied.

Here, we show that obesity drives an abnormal increase in MAM formation, which results in increased calcium flux from the ER to mitochondria in the liver. The mitochondrial calcium overload is accompanied by increased mitochondrial ROS production and impairment of metabolic homeostasis. Suppression of two distinct proteins critical for ER-mitochondrial apposition and calcium flux, IP3R1 (inositol 1,4,5-trisphosphate receptor, type 1) and PACS2 (phosphofurin acidic cluster sorting protein 2), resulted in improved cellular homeostasis and glucose metabolism in obese animals, suggesting that this mechanism is critical for metabolic health and could represent a new therapeutic target for metabolic disease.

Results

Obesity leads to increased ER and mitochondria physical interaction in the liver

In order to investigate ER and mitochondrial morphology and their physical interaction in obesity, we first utilized transmission electron microscopy (TEM) to examine liver sections collected from both genetic (*ob/ob*) and dietary (high-fat diet induced, HFD) models of obesity. In both models this analysis was performed in the context of established obesity, in 8–12 week old *ob/ob* mice and following 16 weeks of HFD feeding. As depicted in figure 1A–D and Fig. S1A and Fig. S1C, we observed that ER membrane displayed a disorganized

morphology in livers derived from obese animals along with a marked increase in ER apposition to mitochondria. Detailed quantitative analysis (described in Fig. S1B) of liver sections from each experimental group (10 sections per animal, 5 different animals per group) demonstrated that the proportion of ER in close contact with mitochondria relative to total ER content was significantly higher in the livers of both *ob/ob* and HFD mice than in lean controls (Fig. 1E). This finding was further substantiated by TEM images of isolated crude mitochondrial pellets that revealed mitochondria of obese animals to be more frequently attached to ER than mitochondria collected from lean controls (Fig. S2A&B). We also employed organelle-targeted fluorescent proteins as an additional strategy to investigate the alterations in ER-mitochondria juxtaposition. For this, we expressed mitochondria-targeted green fluorescent (GFP) and ER-targeted *Discosoma* sp. red fluorescent (DsRed) proteins in the livers of lean and obese mice through adenoviral gene delivery, and performed image analysis in isolated primary hepatocytes from these animals 24 hours after the isolation. We utilized *in vivo* expression of the fluorescent proteins rather than transient transfection following primary cell isolation because hepatocyte metabolism dramatically changes quickly after isolation. As shown in figures 1F and S3A&B, obesity was associated with increased colocalization between ER and mitochondria in liver cells, as revealed by significantly increased Manders' colocalization coefficient between the organelle-targeted fluorescent markers (Fig. 1F and Fig. S3C).

Interestingly, we also observed decreased ER membrane abundance in livers derived from obese animals and a disorganized ER morphology compared with lean counterparts. We performed an extensive morphometric analysis to acquire quantitative comparisons (described in detail Fig. S1B&C). As displayed in figure 1G, ER content was reduced by 50% and 35% in liver cells from *ob/ob* and HFD mice, respectively. This finding is consistent with the measurement of ER area as percentage of total cell area, which was reduced in hepatocytes derived from obese mice (Fig. S1D&E). As an independent read-out of ER content, we also measured calreticulin, a known ER marker, and found that it was decreased in both *ob/ob* and HFD derived livers compared to controls (Fig. S4A). The reduction in ER content in obesity was somewhat surprising since, in the context of ER stress, ER is thought to morphologically rearrange and expand in order to accommodate protein folding demands and re-establish homeostasis[28]. In our analysis, this predicted adaptive response was clearly defective in the context of established obesity. Hepatic mitochondrial content was also reduced in *ob/ob* mice as measured by TEM (Fig. 1H), mtDNA content (Fig. S4B), and COXIV expression (Fig. S4C). In addition, three-dimensional (3D) reconstruction of serial-section TEMs revealed that mitochondria from obese liver were rounder and swollen, compared to the tubular mitochondria observed in the liver of lean animals, in accordance with previous findings[19] (Fig. 1I, Fig. S2C and Movies 1–4). Taken together, our results collected from multiple mouse models through independent means of quantitative analysis indicate that obesity leads to alterations in hepatic ER and mitochondrial structure and enhanced MAM formation.

Next, we asked whether the alterations in ER and mitochondrial morphology and interaction were an early event during the development of obesity or occur as a consequence of the pathological state triggered by overnutrition. We first examined the ER and mitochondrial

morphology by TEM in livers derived from lean and mice fed HFD for just 4 weeks. As can be seen in figure 2A, short term HFD was sufficient to induce ER reorganization, reduction in ER content (Fig. 2B) and a significant increase in ER-mitochondria interactions (Fig. 2C), but did not induce significant changes in total mitochondrial content (Fig. 2D).

In order to determine if changes in ER morphology and MAM content result from ER stress and/or dysfunction, we also examined the effect of acute ER stress in the liver *in vivo* by administration of 0.5μg/kg of tunicamycin (Tm) for 6 and 24 hours in lean mice. As can be seen in figure 2E, tunicamycin treatment resulted in increased phosphorylation of eIF2α and JNK, and upregulated expression of ATF4 and GRP78, classical markers of UPR activation. Interestingly, after 6 hours of Tm treatment we observed a marked increase in MAM formation in the liver (Fig. 2F). This finding is in line with a previous report showing that ER stress induced by Tm induced increased MAM *in vitro*[29]. After 24 hours, however, there were severe structural defects with notable ER dilation and disorganization (Fig. 2F). Taken together, these results suggest that increased MAM formation is a generalized and early response to ER stress.

Obesity leads to upregulation of proteins related to ER-mitochondrial calcium flux

MAMs play a key regulatory role in several cellular functions such as the transfer of Ca^{2+} and lipids from ER to mitochondria[25]. This subdomain of the ER is enriched in specific proteins such as the calcium channel IP3R[30], the mitochondrial-ER tether proteins mitofusin-2[31] and PACS-2[32], chaperones such as sigma 1 receptor[33] and calnexin, and proteins involved in phospholipid metabolism[25] (Fig. 3A). To explore the possible functional consequences of increased ER-mitochondrial contact in obesity, we examined the expression of MAM-enriched proteins in liver lysates from lean and obese mice. As shown in figure 3B, there was a marked upregulation in the expression of proteins involved in Ca^{2+} transport such as IP3R1 and 2 and sigma non-opioid intracellular receptor 1 in samples from obese mice, along with increased content of PACS-2 protein levels. No significant differences were found in mitofusin-2. In these experiments, we validated the specificity or lack there of, the antibodies used in loss-of-function models (Fig. S10). We then performed percoll-based subcellular fractionation of liver tissues to collect enriched fractions of mitochondria, ER and MAM, and verified the preparations by western blot analysis. As can be seen in figure 3C, Cytochrome C is enriched in mitochondrial fractions, IP3R1 and SERCA are preferentially found in the bulk ER, calnexin and PDI are equally distributed between MAM and bulk ER, while sigma1 receptor is found preferentially at the MAM. GRP75, the mitochondrial stress protein, is found mainly in the mitochondria but can also be seen in the MAM fraction as has been described[34]. We then verified that the levels of IP3R1 and 2 were significantly increased in MAMs of obese animals (Fig. 3D). The level of PACS-2 was also increased in samples derived from HFD-fed mice. Although found in similar levels in total lysates, mitofusin-2 was increased in the MAM fractions derived from obese animals, suggesting a possible redistribution of this protein from the mitochondrial membrane to the MAMs. Altogether, these results not only further substantiated our morphological and microscopic observation of an increased number of ER-mitochondrial contact sites in obesity, they also suggest a greater density of anchoring proteins and components involved in Ca^{2+} transport at these sites.

Increased MAM formation correlates with mitochondrial calcium overload in liver derived from obese animals

In MAMs, IP3R resides in close proximity to VDAC, an ion channel located in the outer mitochondrial membrane. This structure facilitates the uptake of Ca^{2+} into the mitochondrial matrix through the low affinity mitochondrial Ca^{2+} uniporter (MCU)[35]. Identifying an increase in MAMs enriched with Ca^{2+} regulatory proteins in fatty livers led us to postulate that abnormal Ca^{2+} transport from ER to mitochondria may occur in obesity, with deleterious consequences for mitochondrial function. To address this hypothesis, we first assessed mitochondrial Ca^{2+} dynamics in obesity by expressing a mitochondria-targeted Ca^{2+} FRET reporter[36] in the liver of lean and obese mice through adeno-associated viral delivery (procedure described in Fig. 4A). Quantitative, single-cell imaging of mitochondrial Ca^{2+} levels in isolated hepatocytes revealed that mitochondria from obese animals contained significantly higher Ca^{2+} ($[Ca^{2+}]$m) at baseline (Fig. 4B). In addition, we detected a higher mitochondrial Ca^{2+} uptake following stimulation of ER Ca^{2+} release with IP3R agonist ATP in primary hepatocytes from obese mice relative to those collected from lean counterparts (Fig. 4C&D). In a complementary approach, we treated primary hepatocytes from lean and obese mice with FCCP, which causes disruption of the mitochondrial membrane potential (MMP) followed by release of mitochondrial Ca^{2+} to the cytosol. As shown in Fig. 4E, addition of FCCP to hepatocytes from obese mice resulted in greater cytosolic Ca^{2+} content compared to lean cells, as measured by Fura2-AM. Notably, the expression of MCU, the mitochondria Ca^{2+} uniporter, was also increased in the ob/ob liver tissue although no difference was found in HFD-fed animals at 16 wks (Fig. S4D). Taken together, these results show that in the setting of obesity, hepatic mitochondria are overloaded with calcium, suggesting a previously unrecognized mechanism of mitochondrial dysfunction in the liver of obese animals. To evaluate whether increased $[Ca^{2+}]$m results from IP3R-mediated ER Ca^{2+} release to the cytosol followed by mitochondrial uptake or by direct transport through MAM junctions, we analyzed cytosolic Ca^{2+} dynamics in response to IP3R stimulation in primary hepatocytes from lean and obese mice using Fura-2AM. As seen in Fig. S5A, baseline cytosolic Ca^{2+} concentration was significantly higher in cells from obese mice. However, ATP stimulation led to similar cytosolic Ca^{2+} rise in hepatocytes from lean and obese animals (Fig. S5B) despite the higher $[Ca^{2+}]$m peak in cells from obese mice (Fig. 4C&D). These observations indicate that in hepatocytes, obesity leads to increased Ca^{2+} transport from the ER through the MAM connections, resulting in elevated mitochondrial Ca^{2+} (Fig. S5C).

Within the mitochondrial matrix, a transient increase in Ca^{2+} level activates matrix enzymes and stimulates oxidative phosphorylation, but sustained exposure to high Ca^{2+} is often detrimental for mitochondrial function[37]. In primary hepatocytes from obese mice we observed decreased basal oxygen consumption and diminished response to the uncoupling agent FCCP, a sign of mitochondrial dysfunction (Fig. 4F&G). Additionally, we observed a moderately but significantly decreased mitochondria membrane potential (Fig. 4H) and increased ROS production (Fig. 4I) in hepatocytes from obese animals, as measured by TMRM and mitosox fluorescence, respectively. These data, together with the altered mitochondrial morphology detected in liver tissue, reveal that in obese animals, high $[Ca^{2+}]$m is associated with mitochondrial dysfunction.

Induced ER-mitochondrial contact by a synthetic linker in the context of obesity results in acceleration of the metabolic perturbations characteristic of obesity

In an attempt to mechanistically connect increased MAM content in obesity with mitochondrial calcium overload, dysfunction and altered cellular and metabolic homeostasis, we asked whether forcing ER-mitochondria interaction per se is sufficient to cause mitochondrial calcium overload and stress in lean, otherwise healthy, animals. To test this hypothesis, we utilized a recombinant construct encoding a synthetic linker[38] that increases ER-mitochondria contact sites (Fig. 5A). In order to validate the efficacy of the construct, we first expressed the linker in hepatocyte-derived mouse Hepa1-6 cells. Twenty-four hours following transfection, the cells were sorted based on RFP fluorescence. TEM analysis confirmed that linker expression significantly increased contact between ER and mitochondria (Fig. 5A). Importantly, these cells remained viable throughout the experiments (48h) with no gross phenotypic changes (Fig. S6A) or signs of cell death as measured by annexin staining followed by FACS analysis (Fig. 5B). Linker expression was associated with increased ATP-stimulated $[Ca^{2+}]m$ rise, in line with increased ER-mitochondrial interactions (Fig. 5C). In addition, this experimental enrichment of ER-mitochondrial contacts led to a modest decrease in basal and maximal mitochondrial respiration (Fig. 5D) accompanied by increased phosphorylation of JNK and expression of CHOP (Fig. S6B), both indicating cellular stress.

We then used adenovirus-mediated gene transfer to express the synthetic linker in the liver of lean animals. Linker expression resulted in increased ER-mitochondrial contact sites in the liver (Fig. S6C). However, in 10-week-old lean mice, linker expression did not appear to have any toxic effects, nor did it cause gross morphological changes within the liver (Fig. S6D) or a metabolic phenotype (Fig. S6E&F). This suggests that in a healthy animal, linker expression was well tolerated and not sufficient to disrupt systemic metabolic homeostasis. However, linker expression in mice following a short period (4 weeks) of high fat diet induced a striking increase in ER-mitochondria contact sites (Fig. 5E and Fig. S7A) and led to significant increase in hepatic lipid accumulation compared with controls (Fig. 5F and Fig. S7B). This was accompanied by decreased mitochondrial oxidative function measured following FCCP treatment (Fig. 5G). At the molecular level, we detected that the linker expression led to activation of JNK, ATF4 and CHOP protein (Fig. 5H) and ATF3 and ATF4 mRNA, with no other changes in UPR markers (Fig. S7C). We also observed impaired insulin-induced phosphorylation of IR, IRS1 and AKT in linker-expressing livers (Fig. S7D), which correlated with a moderate but significant impairment in glucose homeostasis as measured by glucose tolerance (GTT) (Fig. 5I) and with higher liver glucose output as measured by pyruvate tolerance tests (PTT) (Fig. S7E). To explore the whole body glucose fluxes with higher precision, we performed hyperinsulinemic-euglycemic clamp studies. Impaired glucose homeostasis was clearly evident during the clamp experiments in linker-expressing animals, which required significantly lower rates of glucose infusion to sustain euglycemia (Fig. 5J and Fig. S7F–H), indicating that they were relatively insulin insensitive. Clamp hepatic glucose production was significantly increased (Fig. 5J) also indicating impaired hepatic insulin sensitivity. Taken together, these results demonstrate that increasing ER-mitochondrial interaction *in vivo* in a context of mild overnutrition is sufficient to cause mitochondrial dysfunction, activation of stress signaling and impaired

hepatic control of glucose production, accelerating the decline of glucose homeostasis independent of body weight changes (Fig. S7I).

We then asked if modulating mitochondrial Ca^{2+} uptake by other means, such as by experimentally increasing the level of mitochondria calcium uniporter (MCU), previously demonstrated to affect $[Ca^{2+}]m$[39,40] would result in physiological alterations similar to those observed upon increased MAM formation. We found that overexpression of MCU in Hepa1-6 cells led to increased levels of oxidative stress and JNK activation, without inducing cell death (Fig. S8A–C). Taken together these data demonstrate that *in vitro*, $[Ca^{2+}]m$ can be affected either by ER-mitochondrial contact or by expression of MCU, and plays an important role in cellular stress responses.

Down regulation of the IP3R1 calcium channel and the ER-mitochondria tethering protein PACS-2 improves mitochondrial function, decreases cellular stress and improves glucose tolerance in obese mice

Lastly, we asked whether we could improve mitochondrial and cellular function and therefore metabolic homeostasis in obese animals by diminishing ER-mitochondrial Ca^{2+} flux or ER-mitochondrial connection. To this end, we used two different but complementary approaches: we decreased ER-mitochondrial Ca^{2+} fluxes by suppressing hepatic IP3R1, and decreased ER-mitochondrial physical interaction by suppressing hepatic PACS-2 expression. As can be seen in figure 6A, we were able to achieve a 70% reduction in the level of hepatic IP3R1 expression via the delivery of an adenoviral shRNA in mice without influencing the expression levels of other IP3Rs. This resulted in a modest but significant improvement in mitochondrial maximal oxidative capacity (Fig. 6B). In addition, IP3R1 knockdown coincided with decreased stress as measured by pJNK (Fig. 6C), and an improvement in insulin signaling capacity (Fig. 6D). Importantly, these local changes in mitochondrial Ca^{2+} flux in the liver also improved systemic glucose tolerance (Fig. 6E). These findings support our postulate that IP3R1-mediated ER-mitochondrial calcium transport is critical in the maintenance of proper glucose metabolism.

To further explore the functional significance of ER-mitochondria interactions, we targeted PACS2, an integral MAM protein upregulated in obesity (Fig. 3B&E). PACS2 has previously been shown to be involved in MAM formation and inter-organelle communication[32,41]. Using adenoviral shRNA delivery, we achieved nearly 60% knockdown of PACS-2 in *ob/ob* mice (Fig. 6F). Deletion of PACS-2 in cells has been shown to lead to a significant reduction in ER-mitochondria connection and protects against apoptosis[32]. We found that knockdown of PACS-2 resulted in decreased JNK phosphorylation (Fig. 6F) and increased mitochondrial maximal respiration with no alterations in basal mitochondria respiration (Fig. 6G). Reduction of PACS-2 also resulted in improved insulin sensitivity (Fig. 6H), enhanced systemic glucose tolerance (Fig. 6I) and improved liver steatosis (Fig. S8D&E). Taken together, these loss-of-function approaches support the concept that targeting the structural or functional components of MAMs is an effective strategy to improve glucose homeostasis in the context of obesity. Lastly, we asked whether the changes we observed in the context of obesity were unique to the liver. In agreement with previous reports[15,42,43], we found that mitochondrial morphology was

altered in the soleus muscle of ob/ob mice and the expression of MAM-enriched proteins was increased (Supplemental Figure 9), suggesting that the mechanisms described here may also contribute to cellular dysfunction in muscle. However, a more detailed analysis of MAM formation and function in muscle will be required to fully understand the role of these structural changes in insulin resistance in obesity.

Discussion

We have recently shown that aberrant calcium handling in the ER is one of the primary causes of ER dysfunction and stress in obese liver[5]. Here we demonstrate that altered calcium signaling through the MAMs plays a fundamental role in connecting ER stress to mitochondrial dysfunction in obesity, for which plausible mechanisms have been elusive. Our extensive morphological, biochemical and physiological analysis lead us to propose a model in which high nutrient and energy intake leads to increased MAM formation in the liver as an early event in the course of the development of obesity and metabolic disease. Increased MAM formation drives higher calcium accumulation in the mitochondria that in turn leads to impairment in mitochondrial oxidative capacity, increased ROS generation, cellular stress, impaired insulin action in the liver and abnormal glucose metabolism (Fig. 6J).

We have also observed that the induction of acute ER stress such as that triggered by short-term tunicamycin treatment causes a major rearrangement of the ER around the mitochondria, in accordance with earlier findings *in vitro*[29]. These data, together with our findings that the increase in MAM formation is an early event upon high fat diet feeding, suggest that increasing MAM formation may be a short-term adaptive process driven by stress conditions to boost mitochondrial function and lipid synthesis. It is also possible that there are dynamic fluctuations in these interactions during physiological changes in metabolic exposures and ER function to support specific metabolic adaptations.

In obesity however, chronic maintenance of these connections leads to undesirable side effects such as mitochondrial calcium overload. Indeed, in our experiments, increasing MAM formation in the absence of additional stressors was well tolerated and did not affect metabolic homeostasis. However, in the context of even a brief HFD intervention, experimental enrichment of ER-mitochondria interactions accelerated the progression of obesity-related pathology such as hepatic steatosis and glucose intolerance.

The regulation of mitochondrial function by Ca^{2+} is complex and the outcomes for cellular homeostasis depend on the maintenance of $[Ca^{2+}]$ within a very narrow range. Transient fluctuations in mitochondrial calcium stimulate the TCA cycle and oxidative phosphorylation, maintaining optimal cellular bioenergetics[37] Accordingly, cells deficient in all three IP3Rs display compromised mitochondrial function as a result of diminished mitochondrial Ca^{2+} uptake[44]. Also, interventions that decrease ER-mitochondrial interaction below physiological thresholds, such as tissue-specific deletion of mitofusin-2 in liver[45] and hypothalamus[46] lead to mitochondrial dysfunction and insulin and leptin resistance, respectively. Although these experiments do not specifically address the regulation of ER-mitochondria Ca^{2+} flux due to the pleiotropic functions of the targeted molecules, they

indicate that the proper maintenance of MAMs and Ca^{2+} flux is essential for mitochondrial function and metabolic homeostasis.

We also showed here that the down regulation of key molecules involved in ER-mitochondria connection and calcium flux such IP3R1 and PACS-2 results in improved mitochondrial respiration, decreased cellular stress, and enhanced glucose tolerance in obese animals. It is important to note that both IP3R1 and PACS-2 are not exclusively expressed in the MAM, and thus targeting these molecules may result in alterations to cellular function outside the MAM. For example, it is known that IP3R1 also regulates cytosolic Ca^{2+} flux, thus alternative explanations for our observation of improved glucose homeostasis following IP3R knockdown should be considered. Indeed, it was recently reported that in the liver, IP3R regulates systemic glucose metabolism by increasing cytosolic calcium and glucagon signaling in the hepatocyte, and reduced IP3R1 consequently decreased glucose production[47,48]. These results are consistent with our findings. However, the effects of hepatic IP3R1 suppression on OCR shown here (Fig. 6B) strongly suggest that altered mitochondrial function also significantly contributes to the metabolic phenotype *in vivo*. Furthermore, producing metabolic improvements by these two independent interventions modulating different aspects of ER-mitochondria interactions strongly support their importance in organelle and metabolic homeostasis.

The effect of MAM regulation on metabolism is likely to result from the engagement of multiple pathways and multiple structural components. Interventions that disrupt individual MAM components may thus only partially recapitulate the impact of overall MAM function in cellular and organismal physiology. Also, MAM regulation impacts not only calcium flux but also lipid biosynthesis, autophagy and mitochondrial fission[25–27]. Since all of these phenomena are altered in obesity it is possible that alteration of MAMs has a more pleiotropic effect in the obese condition as well as stage-specific metabolic pathologies mediated distinctly by different molecular components, and these processes should be explored in future studies. During the review of this manuscript, an independent group reported that HFD feeding leads to diminished ER-mitochondria contact sites in liver and primary hepatocytes[49]. It is important to note that MAM formation and content in the liver exhibit high level of plasticity depending on metabolic status, age, and stress condition, and thus the contrasting conclusions may reflect both differing experimental parameters and analytical methodology including in vitro assays. Since liver size and lipid content increase in obesity, total MAM content should be evaluated relative to alterations in tissue mass and composition. These issues notwithstanding, cumulative evidence support the concept the MAM regulation has a major impact on glucose homeostasis [44,50].

The association between defective mitochondrial function, insulin resistance and type 2 diabetes has been a topic of intense investigation and debate in the field[45,46,50]. Most studies have been performed in human skeletal muscle where insulin resistance is linked to impaired mitochondrial oxidative function and density[14,20]. However, whether these alterations cause or result from insulin resistance is presently unclear. As we found that skeletal muscle mitochondrial morphology is altered in soleus muscle of ob/ob mice and expression of MAM-enriched proteins is increased, altered SR-mitochondria calcium fluxes may also play a role in obesity-related mitochondrial dysfunction in muscle.

Our observations may have implications beyond obesity. Enhanced MAM function and increased ER–mitochondrial interaction have been observed in neurodegenerative diseases such as gangliosidosis[50], Alzheimer's disease[51] and also in senescence[52]. Notably, Alzheimer's disease is also associated with insulin resistance in the brain[53] and shares numerous molecular features with obesity including ER stress, JNK activation, and organelle dysfunction as well as aging. Therefore, we suggest that therapies that restore the proper function of ER-mitochondrial interface may be a useful approach in the treatment of multiple metabolic diseases with these mechanistic features.

Online Methods

Animals

Male leptin deficient (*ob/ob*) and wild type littermates in the C57BL/6J background at 6 weeks of age were obtained from Jackson Laboratories (strain B6.V-Lepob/J, stock number 000632). For the diet-induced obesity model, male C57BL/6J mice were purchased from Jackson Labs and were placed on HFD (D12492: 60% kcal% fat; Research Diets). All mice were maintained from 4–10 weeks on a 12-hour-light/12-hour-dark cycle in a pathogen-free barrier facility with free access to water and food. The Harvard Medical Area Standing Committee on Animals approved all *in vivo* studies. Sample size was chosen based on pilot experiments that ensured a power of 90% and a significance level of 5%. All samples were included in analysis unless they fell more than two standard deviations from the mean. No randomization was used for animal studies.

Transmission Electron microscopy: Fixation

Whole liver tissue and skeletal muscle: 8–10 week old wt and *ob/ob* mice and 4 and 16 week old HFD fed mice and controls were anesthetized with 2mg/ml xylazine and 2mg/ml ketamine and perfused with saline and then with fixative buffer containing: 2.5% glutaraldehyde, 2.5% paraformaldehyde in 0.1 M sodium cacodylate buffer (pH 7.4). After perfusion, small pieces (1–2mm cubes) of liver and skeletal muscle were immersed in the same fixative buffer described above for at least 2 hours at 4°C. The tissues were washed in 0.1M cacodylate buffer and postfixed with 1% Osmiumtetroxide (OsO$_4$)/1.5% Potassiumferrocyanide (K$_2$FeCN$_6$) for 1 hour, washed in water three times and incubated in 1% uranyl acetate in maleate buffer for 1hr followed by 3 washes in maleate buffer and subsequent dehydration in grades of alcohol (10min each; 50%, 70%, 90%, 2×10min 100%). The following day, samples were embedded in TAAB 812 Resin mixture and polymerized at 60°C for 48 hrs. Mitochondrial pellets and cells: Mitochondria preparation was performed as described in the subcellular fractionation section. Pellets were resuspended in a 1:1 ratio in a fixative buffer. The fixative contains 4 parts a stock (2.5% PFA, 0.06% picric acid in 0.2M Sodium Cacodylate buffer pH 7.4) and 1 part of 25% glutaraldehyde. In the case of cells, the fixative was diluted in growth media (DMEM) in a 1:1 ratio and layered on top of the cells. Cells were maintained in fixative for at least 2 hours. The samples were then placed in propyleneoxide for 1 hr and infiltrated in a 1:1 mixture of propyleneoxide and TAAB 812 Resin mixture (Marivac Canada Inc. St. Laurent, Canada). **Sectioning, imaging and quantification**: Ultrathin sections (about 90nm) were generated using a Reichert Ultracut-S microtome, picked up on to copper grids, stained with lead citrate and examined

in a TecnaiG″ Spirit BioTWIN microscope. Images were recorded with an AMT 2k CCD camera. Given the known variability of TEM we set out a very thorough quantitative analysis. For that, 50 pictures of each experimental group (from 5 different animals per group) were obtained at 6800x magnification. The pictures were taken from the same liver lobe. The images were analyzed using Image J (National Institutes of Health, USA). The mitochondrial and ER membranes were delineated using the freehand tool. The selected areas were converted to masks and total number, area, perimeter of ER and mitochondria were calculated. Two independent investigators quantified the images blindly. For the acquisition of MAM quantification, we normalized the total ER connected to mitochondria either to total ER perimeter and total mitochondrial perimeter. Because we verified that the total ER mass and mitochondria content were both decreased in obesity, the normalization is necessary to acquire accurate measurements. For the single cell quantification, pictures were taken at 1400 or 1900x magnification. The images (five of each) were analyzed using the IMOD software. Cell membrane, lipid droplets, nucleus, mitochondrial and ER membranes were drawn as separate contours. Area and perimeter values were calculated by using 'imodinfo' function.

Serial EM and reconstruction

For the serial 3D EM reconstruction, serial sections were generated 60nm apart and aligned in a grid. The pictures were taken at 11000x magnification in the exact same field in each section, based on the location of the nucleus. The images in the stack were aligned by the auto alignment tool of the IMOD Etomo software (The Boulder Laboratory for 3D Electron Microscopy of Cells, CO). Aligned pictures were interpolated in ImageJ. Each mitochondrion, cristae and ER were drawn as separate contours. Each object was tracked in consecutive pictures. 3D segmentation was generated using IMOD 3dMOD software.

Confocal imaging

For confocal imaging, adenoviruses expressing acGFP fused with a targeting sequence of subunit IV of COX (from Clontech) and DsRed fused with calreticulin targeting and to the KDEL retention sequences for ER (from Clontech) were intravenously injected into mice at a titer of 1.0×10^9 IFU/mice. One week after the injection, primary hepatocytes were isolated from wt and *ob/ob* mice and seeded onto a 3.5-mm round glass dishes (1.5mm) and left overnight at 37°C, 5%CO$_2$. The following morning cells were washed and placed in hanks balanced salt solution (HBSS) supplemented with 10 mM Hepes. The cells were imaged with a Yokogawa CSU-X1 spinning disk confocal system (Andor Technology, South Windsor, CT), attached to a Nikon Ti-E inverted microscope (Nikon Instruments, Melville, NY). Laser excitation of GFP and DsRed was performed sequentially using the 488nm and 561nm lasers, respectively. Images were acquired using a 60x Plan Apo objective lens with a Hamamatsu OrcaER camera. Acquisition parameters, shutters, filter positions and focus were controlled by Andor iQ software (Andor Technology, South Windsor, CT). For confocal *z*-axis stacks, 40 images separated by 0.27 μm along the *z*-axis were acquired. WCIF Image J has been used to determine the manders' colocalization coefficients of the mitochondria - ER interaction, and the Volume J plugin for Image J was used for the 3D reconstruction and surface rendering. Confocal microscopy images for this

study were acquired in the Confocal and Light Microscopy Core Facility at the Dana Farber Cancer Institute.

Tunicamycin (Tm) treatment

8 week old lean C57B6/J mice were injected intraperitoneally with Tm (0.5μg/g body weight in 150mM dextrose) or vehicle (150 mM dextrose), and liver tissue was isolated at 6 h and 24h after the injection. Animals were fed ad libidum during this time.

Mitochondria membrane potential

Mitochondrial membrane potential (Δψ) was measured by loading cells with 10 nM tetramethyl rhodamine methyl ester (TMRM, Invitrogen) for 30 min at 37 °C. Images were taken on a Nikon inverted TE2000 microscope equipped with a Hamamatsu Orca ER digital camera. TMRM excitation was 560 nm and emission was 590–650 nm. Images were obtained every 10 s with a fixed 200 ms exposure time. FCCP (1μM) was added after 12 pictures to disrupt the Δψ.

Subcellular Fractionation

The subcellular fractionation of the liver was performed based on published protocols[54] with minor modifications. 8–10 week wt, *ob/ob* mice and 16 weeks HFD-fed and lean controls were fasted overnight in order to deplete glycogen stocks. The following morning, the animals were sacrificed and 1g of liver was immediately weighed and washed 3 times in cold Buffer 1 (content described below). The tissue was minced and immersed in Buffer 2. The tissue was filtered to eliminate the blood and transferred to a glass potter in 30mL of Buffer 1 and further disrupted by Dounce homogenization. The homogenate was centrifuged at 740*g* for 5 min twice in a Sorvall instrument; the supernatant was recovered and further centrifuged for 10 min at 8000*g,* 3 times. The resulting pellet (crude mitochondrial fraction) (Supplementary Fig. 3) was collected and the supernatant was saved for gathering the ER fraction. The crude mitochondrial fraction was layered in a 30% Percoll gradient in Buffer 3 and centrifuged at 95000*g* for 30 minutes using a Beckman ultracentrifuge in a 41.1 SW rotor. The obtained pure mitochondrial fraction was recovered at the bottom of the tube while the mitochondrial-associated membranes (MAMs) were identified as an intermediate layer between the light membrane and the pure mitochondrial fractions. The pure mitochondria fraction was collected, diluted in MRB buffer and further centrifuged at 10.000g (11300 rpm). The pellet was re-suspended in 2mL of MRB buffer. The MAM fraction was collected and diluted 10x in MRB buffer. The suspension was centrifuged 100.000g in a Beckman instrument. The pellet was re-suspended in small volume of MRB buffer. The ER fraction was obtained by centrifuging the supernatant collected from the 8.000g centrifugation step at 100.000g for 60 min. Protein concentration was determined by BCA and 25μg of protein were separated by SDS-PAGE and immunoblotted as indicated in the figure legends. Buffer1: Manitol 225mM, Sucrose 75mM, Tris-HCl 30mM, BSA 0.5% and EGTA 0.5mM, pH7.4. Buffer2: Manitol 225mM, Sucrose 75mM, Tris-HCl 30mM, BSA 0.5%, pH 7.4. Buffer3: Manitol 225mM, Sucrose 75mM, Tris-HCl 30mM, pH 7.4. MRB Buffer: Manitol 225mM, Hepes 5mM, EGTA 0.5mM, pH 7.4.

Total protein extraction and western blotting

For preparation of total cellular proteins, liver and skeletal muscle tissues were homogenized in cold lysis buffer containing 50 mM Tris-HCl (pH 7.4), 2 mM EGTA, 5 mM EDTA, 30 mM NaF, 10 mM Na_3VO_4, 10 mM $Na_4P_2O_7$, 40 mM glycerophosphate, 1% NP-40, and 1% protease inhibitor cocktail. The total homogenate was centrifuged 9000rpm for 15 minutes to pellet cell debris. Protein concentration was determined in the supernatant by BCA and 1/5 volume of 5x Laemmli buffer was added into the whole cell lysate that was boiled for 5 minutes afterwards. Proteins were subjected to SDS-polyacrylamide gel electrophoresis, as previously described[9]. Membranes were incubated with anti-IP3R1, anti-IP3R2 (kind gift from Dr. Richard Wojcikiewicz and acquired from Thermo-scientific PA1-901, respectively), anti-Mitofusin 2 (Abcam ab56889 and Sigma M6319), anti-sigma 1 receptor (Oprs1, Abcam 53852) anti-SERCA2b (Cell signaling #4388), anti-MCU (Sigma HPA016480), anti-PDI (Cell signaling #2446), anti-pJNK (Cell signaling #81E11), anti-P-eIF2alpha (Cell signaling #3597), anti-CHOP (Cell signaling mab# 2895), anti-pAKT (Santa cruz 7985R), anti-AKT (Santa cruz 8312), anti-IR (Santa cruz 711), pIR (Calbiochem 407707), anti-IRS1 (Santa cruz 559G); anti-pY20 (Santa cruz -508), anti-RFP (ab62341), anti PACS-2 was kind gift from Dr. Gary Thomas. All the antibodies were incubated overnight at 4°C. The PVDF membranes were incubated with the secondary antibody conjugated with horseradish peroxidase (Amersham Biosciences) and were visualized using the enhanced chemiluminescence system (Roche Diagnostics). The validation of IP3R1, PACS-2, Sigma 1R and mitofusin-2 antibodies were determined by knockdown and overexpression (Figure S10).

Primary hepatocyte isolation

For the isolation of primary hepatocytes, 8–10 weeks old wt and *ob/ob* mice were anesthetized by 2mg/ml xylazine and 2mg/ml ketamine. The liver was perfused through the portal vein with 10–15mL of warm (37°C) HBSS buffer (Invitrogen, CA) supplemented with 1 mM EGTA and 5mM of glucose, and then digested with 10–15mL of Collagenase X (WAKO, Japan) at 0.3mg/mL dissolved in HBSS buffer supplemented with 1.2mM $CaCl_2$ and 5 mM glucose. After perfusion, primary hepatocytes were released and sedimented at 500 rpm for 2 minutes and washed two times with medium 199 (Invitrogen, CA). Hepatocytes were then layered on a 70% (for wt) and 50% (for *ob/ob*) Percoll gradient and centrifuged 2000 rpm for 10 minutes. The healthy cells were recovered at the bottom of the tube.

Mitochondrial oxygen consumption

Real time mitochondrial oxygen consumption rate was measured using the XF24 extracellular flux analyzer from Seahorse Biosciences. Hepatocytes were seeded on collagen-coated XF24 plates (Seahorse Bioscience, MA) at 4×10^4 cells/well. For Hepa1-6, cells were seeded at 4×10^4 cells/well in non-coated plates. Cells were kept overnight in normal growth medium and then rinsed twice and kept in 600μl of sodium bicarbonate-free DMEM medium (Sigma, MO) supplemented with 20mM glucose and 1mM sodium pyruvate. The respiratory rate was measured at 37°C in 8 replicates (independent wells) for

each of the plates of pairs of lean and obese mice. OCR rates were calculated and analyzed using the Seahorse XF24 v1.7.0.74 software[55].

Ca^{2+} imaging

FRET Mitochondria Ca^{2+} measurements: The plasmid expressing 4mtD3cpv was kindly provided by Roger Tsien (Un. Of California, San Diego) and cloned into an Adeno-associated virus expression system (AAV-serotype DJ). The AAV was injected intravenously into mice. After 10–15 days, primary hepatocytes were isolated and seeded onto 3.5cm imaging dishes at the density of 40K per dish and incubated overnight at 37°C. Hepa 1-6 cells were seeded on 3.5-cm imaging dishes and transiently transfected with 4mtD3cpv plasmid using lipofectamine overnight. 48 hours after transfection, imaging was performed after washing and maintenance in a medium containing 10 mM Hepes, 150mM NaCl, 4mM KCl, 2mM CaCl$_2$, 1mM MgCl$_2$, 10mM D-glucose, pH 7.4. Ca^{2+}-free medium were prepared similarly as above, in the absence of CaCl$_2$ and adding 2mM EGTA and 3 mM MgCl$_2$. Fluorescent images of single cells were obtained using an Olympus IX81 microscope and an ORCA-AG camera from Humamatsu with a filter cube Chroma 71007A. Emission ratio of the Cameleon was obtained by using two emission filters (485/40 for CFP and 535/25 for citrine) controlled by a Lambda 10-2 filter changer (Sutter Instruments, Novato, CA). Exposure times were typically 250ms and images were collected every 5 seconds, background corrected and analyzed with Slidebook (Intelligent Imaging Innovations).

Cytosolic Ca^{2+}

Cytosolic Ca^{2+} levels were determined using Fura-2 AM (Invitrogen). Briefly, cells were loaded with 4μM Fura-2AM and 1uM Pluronic F-127 in HBSS for 60 min at room temperature and then washed and maintained in the same buffer described for mitochondria Ca^{2+} measurements. Fluorescence images were obtained using an Olympus IX70 with 40x objective and alternatively illuminated with 340 and 380 nm light for 250ms (Lambda DG-4; Sutter Instrument Co.). Emission light > 510 nm was captured using a CCD camera (Orca-ER; Hamamatsu Photonics). Images were collected every 5 seconds, background corrected and analyzed with Slidebook.

ROS production

Primary hepatocytes were isolated as described above. One day after isolation, cells were washed and incubated for 30 min at 37° C with 3μM of mitosox in a medium containing: NaCl 121mM, NaHCO$_3$, Hepes 10mM, KCl 4.7mM, KH$_2$PO$_4$, MgSO$_4$, CaCl$_2$, glucose 10mM and dextran at 2%. Signal was quantified in Image J.

Cell culture, linkers and MCU

The control and linker plasmids were kindly provided by Dr. György Hajnóczky from Thomas Jefferson University. MCU-V5-His in pDEST 40 vector was obtained form Addgene (plasmid # 31731). The linker used in these experiments was designed to link ER and mitochondria to a 20–30 nm proximity. Hepa 1-6 cells (a mouse hepatocyte cell line from ATCC) were transfected with 1μg DNA of the control construct (the same construct as

the linker lacking the ER targeting sequence) and the linker with lipofectamine LTX (Invitrogen) overnight in Optimem (Gilbco). After transfection cells were incubated in growth media (DMEM and 10% CCS). For EM and seahorse experiments, 24 hours after transfection cells were sorted in a cell sorter based on RFP fluorescence. The positive cells were plated and used for experiments the next day. For western blot experiments, cells were transfected and 48 hours later harvested and lysed with NP40 1% buffer. For insulin signaling experiments, cells were serum deprived for 4 hours before the experiment and then stimulated with 3nM insulin for 3 minutes.

Cell death assay

The Annexin-V-FITC Apoptosis Detection Kit (BD Biosciences) was used to detect apoptosis by flow cytometry. Cells were transfected with control and linkers and harvested after 48 h and processed according to the manufacturer's instructions.

Adenovirus-mediated expression of linkers

For *in vivo* linker experiments, the construct was cloned into an adenovirus backbone (serotype 5, Ad5, vector biolabs) under the CMV promoter. Adenovirus was amplified in 293A cells, purified twice using CsCl column, desalted, and $1x\ 10^9$ IFU/mouse were injected intravenously. Adenovirus transductions of mice were performed between 8–10 weeks of age. For histological analysis, liver tissues were fixed in 10% formalin solution, and sectioned for Hematoxylin and Eosin staining. For EM, confocal and seahorse experiments, hepatocytes were isolated after 7 days of adenovirus infection.

Adenovirus-mediated knockdown of PACS-2 and IP3R1

For the loss of function experiments using shRNA, 5 shRNA sequences against mouse IP3R1 and PACS-2 were obtained from MISSION shRNA Library (Sigma). Knockdown efficiency of each was first tested *in vitro* and the most effective sequences were selected to clone into an adenovirus backbone (serotype 5, Ad5, Vector biolabs) under the U6 promoter. The adenoviruses were injected intravenously in a titer of 1×10^9 IFU/mouse for IP3R1 and 5×10^8 IFU/mouse for PACS-2. The metabolic experiments were performed after 8–10 days of infection and the animals were sacrificed after 14 days of infection for ex vivo experiments.

Glucose and insulin tolerance tests and insulin infusions

Glucose tolerance tests were performed by intraperitoneal glucose injection (1.5 g kg^{-1}) after an overnight fast, and insulin tolerance tests were performed by intraperitoneal insulin injection (1IU kg^{-1}) after a 6 hr food withdrawal[56]. For the insulin infusions, following 6 hr of food withdrawal, obese mice were anaesthetized with an intraperitoneal injection of 2mg/ml xylazine and 2mg/ml ketamine, and insulin (1 IU kg^{-1}) or phosphate buffered saline (PBS) in 200 ml volume was infused into the portal vein. Three minutes after infusion, tissues were removed and frozen in liquid nitrogen and kept at −80°C until processing.

Hyperinsulinemic euglycemic clamp studies

Seven days before the experiments the animals were injected intravenously with adenovirus expressing a control or the synthetic linker at a titer of 0.5 to 1×10^9 IFU/mouse. Seven days after infection and four days prior to experiments, mice were anesthetized, and the right jugular vein was catheterized with a PE-10 polyethylene tube (inside and outside diameters, 0.28mm and 0.61mm, respectively; Becton Dickinson) filled with heparin solution (100USP U/ml). The distal end of the catheter was tunneled under the skin, exteriorized in the intrascapular area, heat sealed, and then placed in a pocket under the skin until the day of the experiment, when it was re-exteriorized. Hyperinsulinemic-euglycemic clamps were performed by modification of reported procedures [56][56,57]. Steady-state tracer analysis was used for calculations, and glucose-specific activity was verified for steady state.

Supplementary Material

Refer to Web version on PubMed Central for supplementary material.

Acknowledgments

References

1. Flegal KM, Carroll MD, Ogden CL, Curtin LR. Prevalence and trends in obesity among US adults, 1999–2008. JAMA: the journal of the American Medical Association. 2010; 303:235–241.

2. Hotamisligil GS. Inflammation and metabolic disorders. Nature. 2006; 444:860–867. [PubMed: 17167474]

3. Hotamisligil GS. Endoplasmic reticulum stress and the inflammatory basis of metabolic disease. Cell. 2010; 140:900–917. [PubMed: 20303879]

4. Lowell BB, Shulman GI. Mitochondrial dysfunction and type 2 diabetes. Science. 2005; 307:384–387. [PubMed: 15662004]

5. Fu S, et al. Aberrant lipid metabolism disrupts calcium homeostasis causing liver endoplasmic reticulum stress in obesity. Nature. 2011; 473:528–531. [PubMed: 21532591]

6. Otoda T, et al. Proteasome dysfunction mediates obesity-induced endoplasmic reticulum stress and insulin resistance in the liver. Diabetes. 2013; 62:811–824. [PubMed: 23209186]

7. Walter P, Ron D. The unfolded protein response: from stress pathway to homeostatic regulation. Science. 2011; 334:1081–1086. [PubMed: 22116877]

8. Ozcan L, Tabas I. Role of endoplasmic reticulum stress in metabolic disease and other disorders. Annual review of medicine. 2012; 63:317–328.

9. Boden G, et al. Increase in endoplasmic reticulum stress-related proteins and genes in adipose tissue of obese, insulin-resistant individuals. Diabetes. 2008; 57:2438–2444. [PubMed: 18567819]

10. Gregor MF, et al. Endoplasmic reticulum stress is reduced in tissues of obese subjects after weight loss. Diabetes. 2009; 58:693–700. [PubMed: 19066313]

11. Ozcan U, et al. Chemical chaperones reduce ER stress and restore glucose homeostasis in a mouse model of type 2 diabetes. Science. 2006; 313:1137–1140. [PubMed: 16931765]

12. Kars M, et al. Tauroursodeoxycholic Acid may improve liver and muscle but not adipose tissue insulin sensitivity in obese men and women. Diabetes. 2010; 59:1899–1905. [PubMed: 20522594]

13. Xiao C, Giacca A, Lewis GF. Sodium phenylbutyrate, a drug with known capacity to reduce endoplasmic reticulum stress, partially alleviates lipid-induced insulin resistance and beta-cell dysfunction in humans. Diabetes. 2011; 60:918–924. [PubMed: 21270237]

14. Zhang D, et al. Mitochondrial dysfunction due to long-chain Acyl-CoA dehydrogenase deficiency causes hepatic steatosis and hepatic insulin resistance. Proceedings of the National Academy of Sciences of the United States of America. 2007; 104:17075–17080. [PubMed: 17940018]

15. Kelley DE, He J, Menshikova EV, Ritov VB. Dysfunction of mitochondria in human skeletal muscle in type 2 diabetes. Diabetes. 2002; 51:2944–2950. [PubMed: 12351431]

16. Kim JA, Wei Y, Sowers JR. Role of mitochondrial dysfunction in insulin resistance. Circulation research. 2008; 102:401–414. [PubMed: 18309108]

17. Petersen KF, et al. Mitochondrial dysfunction in the elderly: possible role in insulin resistance. Science. 2003; 300:1140–1142. [PubMed: 12750520]

18. Vianna CR, et al. Hypomorphic mutation of PGC-1beta causes mitochondrial dysfunction and liver insulin resistance. Cell metabolism. 2006; 4:453–464. [PubMed: 17141629]

19. Cheng Z, et al. Foxo1 integrates insulin signaling with mitochondrial function in the liver. Nature medicine. 2009; 15:1307–1311.

20. Patti ME, Corvera S. The role of mitochondria in the pathogenesis of type 2 diabetes. Endocrine reviews. 2010; 31:364–395. [PubMed: 20156986]

21. Mantena SK, King AL, Andringa KK, Eccleston HB, Bailey SM. Mitochondrial dysfunction and oxidative stress in the pathogenesis of alcohol- and obesity-induced fatty liver diseases. Free radical biology & medicine. 2008; 44:1259–1272. [PubMed: 18242193]

22. Bugianesi E, et al. Insulin resistance in non-diabetic patients with non-alcoholic fatty liver disease: sites and mechanisms. Diabetologia. 2005; 48:634–642. [PubMed: 15747110]

23. Vial G, et al. Effects of a high-fat diet on energy metabolism and ROS production in rat liver. Journal of hepatology. 2011; 54:348–356. [PubMed: 21109325]

24. Begriche K, Massart J, Robin MA, Bonnet F, Fromenty B. Mitochondrial adaptations and dysfunctions in nonalcoholic fatty liver disease. Hepatology. 2013; 58:1497–1507. [PubMed: 23299992]

25. Rowland AA, Voeltz GK. Endoplasmic reticulum-mitochondria contacts: function of the junction. Nature reviews Molecular cell biology. 2012; 13:607–625.

26. Hamasaki M, et al. Autophagosomes form at ER-mitochondria contact sites. Nature. 2013; 495:389–393. [PubMed: 23455425]

27. Friedman JR, et al. ER tubules mark sites of mitochondrial division. Science. 2011; 334:358–362. [PubMed: 21885730]

28. Schuck S, Prinz WA, Thorn KS, Voss C, Walter P. Membrane expansion alleviates endoplasmic reticulum stress independently of the unfolded protein response. The Journal of cell biology. 2009; 187:525–536. [PubMed: 19948500]

29. Bravo R, et al. Increased ER-mitochondrial coupling promotes mitochondrial respiration and bioenergetics during early phases of ER stress. Journal of cell science. 2011; 124:2143–2152. [PubMed: 21628424]

30. Pinton P, Giorgi C, Siviero R, Zecchini E, Rizzuto R. Calcium and apoptosis: ER-mitochondria Ca2+ transfer in the control of apoptosis. Oncogene. 2008; 27:6407–6418. [PubMed: 18955969]

31. de Brito OM, Scorrano L. Mitofusin 2 tethers endoplasmic reticulum to mitochondria. Nature. 2008; 456:605–610. [PubMed: 19052620]

32. Simmen T, et al. PACS-2 controls endoplasmic reticulum-mitochondria communication and Bid-mediated apoptosis. The EMBO journal. 2005; 24:717–729. [PubMed: 15692567]

33. Hayashi T, Su TP. Sigma-1 receptor chaperones at the ER-mitochondrion interface regulate Ca(2+) signaling and cell survival. Cell. 2007; 131:596–610. [PubMed: 17981125]

34. Szabadkai G, et al. Chaperone-mediated coupling of endoplasmic reticulum and mitochondrial Ca2+ channels. The Journal of cell biology. 2006; 175:901–911. [PubMed: 17178908]

35. Rizzuto R, et al. Ca(2+) transfer from the ER to mitochondria: when, how and why. Biochimica et biophysica acta. 2009; 1787:1342–1351. [PubMed: 19341702]

36. Palmer AE, Tsien RY. Measuring calcium signaling using genetically targetable fluorescent indicators. Nature protocols. 2006; 1:1057–1065.

37. Rizzuto R, De Stefani D, Raffaello A, Mammucari C. Mitochondria as sensors and regulators of calcium signalling. Nature reviews Molecular cell biology. 2012; 13:566–578.

38. Csordas G, et al. Structural and functional features and significance of the physical linkage between ER and mitochondria. The Journal of cell biology. 2006; 174:915–921. [PubMed: 16982799]

39. De Stefani D, Raffaello A, Teardo E, Szabo I, Rizzuto R. A forty-kilodalton protein of the inner membrane is the mitochondrial calcium uniporter. Nature. 2011; 476:336–340. [PubMed: 21685888]

40. Baughman JM, et al. Integrative genomics identifies MCU as an essential component of the mitochondrial calcium uniporter. Nature. 2011; 476:341–345. [PubMed: 21685886]

41. Lynes EM, Simmen T. Urban planning of the endoplasmic reticulum (ER): how diverse mechanisms segregate the many functions of the ER. Biochimica et biophysica acta. 2011; 1813:1893–1905. [PubMed: 21756943]

42. Jheng HF, et al. Mitochondrial fission contributes to mitochondrial dysfunction and insulin resistance in skeletal muscle. Molecular and cellular biology. 2012; 32:309–319. [PubMed: 22083962]

43. Bonnard C, et al. Mitochondrial dysfunction results from oxidative stress in the skeletal muscle of diet-induced insulin-resistant mice. The Journal of clinical investigation. 2008; 118:789–800. [PubMed: 18188455]

44. Cardenas C, et al. Essential regulation of cell bioenergetics by constitutive InsP3 receptor Ca2+ transfer to mitochondria. Cell. 2010; 142:270–283. [PubMed: 20655468]

45. Sebastian D, et al. Mitofusin 2 (Mfn2) links mitochondrial and endoplasmic reticulum function with insulin signaling and is essential for normal glucose homeostasis. Proceedings of the National Academy of Sciences of the United States of America. 2012; 109:5523–5528. [PubMed: 22427360]

46. Schneeberger M, et al. Mitofusin 2 in POMC neurons connects ER stress with leptin resistance and energy imbalance. Cell. 2013; 155:172–187. [PubMed: 24074867]

47. Ozcan L, et al. Calcium signaling through CaMKII regulates hepatic glucose production in fasting and obesity. Cell metabolism. 2012; 15:739–751. [PubMed: 22503562]

48. Wang Y, et al. Inositol-1,4,5-trisphosphate receptor regulates hepatic gluconeogenesis in fasting and diabetes. Nature. 2012; 485:128–132. [PubMed: 22495310]

49. Tubbs E, et al. Mitochondria-Associated Endoplasmic Reticulum Membrane (MAM) Integrity Is Required for Insulin Signaling and Is Implicated in Hepatic Insulin Resistance. Diabetes. 2014

50. Sano R, et al. GM1-ganglioside accumulation at the mitochondria-associated ER membranes links ER stress to Ca(2+)-dependent mitochondrial apoptosis. Molecular cell. 2009; 36:500–511. [PubMed: 19917257]

51. Area-Gomez E, et al. Upregulated function of mitochondria-associated ER membranes in Alzheimer disease. The EMBO journal. 2012; 31:4106–4123. [PubMed: 22892566]

52. Cali T, Ottolini D, Brini M. Mitochondrial Ca(2+) and neurodegeneration. Cell calcium. 2012; 52:73–85. [PubMed: 22608276]

53. Bomfim TR, et al. An anti-diabetes agent protects the mouse brain from defective insulin signaling caused by Alzheimer's disease- associated Abeta oligomers. The Journal of clinical investigation. 2012; 122:1339–1353. [PubMed: 22476196]

54. Wieckowski MR, Giorgi C, Lebiedzinska M, Duszynski J, Pinton P. Isolation of mitochondria-associated membranes and mitochondria from animal tissues and cells. Nature protocols. 2009; 4:1582–1590.

55. Wu M, et al. Multiparameter metabolic analysis reveals a close link between attenuated mitochondrial bioenergetic function and enhanced glycolysis dependency in human tumor cells. American journal of physiology Cell physiology. 2007; 292:C125–136. [PubMed: 16971499]

56. Furuhashi M, et al. Treatment of diabetes and atherosclerosis by inhibiting fatty-acid-binding protein aP2. Nature. 2007; 447:959–965. [PubMed: 17554340]

57. Rossetti L, et al. Peripheral but not hepatic insulin resistance in mice with one disrupted allele of the glucose transporter type 4 (GLUT4) gene. The Journal of clinical investigation. 1997; 100:1831–1839. [PubMed: 9312184]
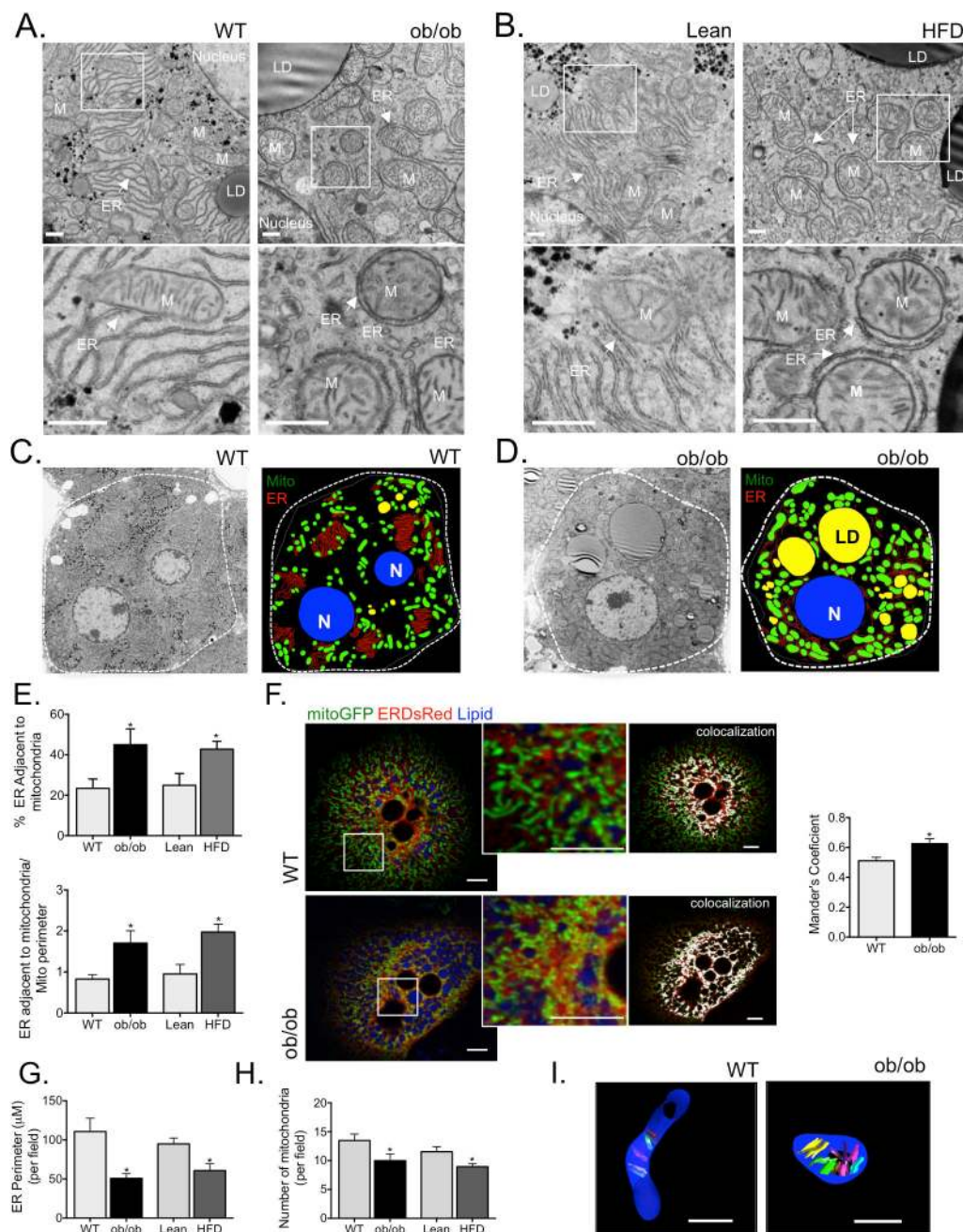
Figure 1. Obesity induces increased MAM formation and changes in ER and mitochondrial morphology in the liver

(A&B) Representative transmission electron microscopy (TEM) of liver sections derived from wild type and leptin-deficient (wt and *ob/ob,* 8–10 weeks of age, A) or lean and obese (16 weeks of high fat diet, HFD, B) mice at 6800x, scale bar 500nm. ER (endoplasmic reticulum), M (mitochondria), N (nucleus), LD (lipid droplet). (C&D) TEM images were analyzed using iMOD to delineate major cellular structures at 1400x. (E) Quantitation of ER length adjacent to mitochondria normalized by total ER length and by mitochondrial perimeter. (F) Confocal images of primary hepatocytes isolated from lean (wt) and obese

(*ob/ob)* mice co-expressing a mitochondria-targeted GFP (mito-GFP), an ER-targeted DsRed (ER-DsRed) and stained with a lipid droplet specific dye (monodansylpentane). (F) Statistical quantification of the overlapping area (Manders' coefficient) between Mito-GFP and ER-DsRed, n=10 (wt) n=11 (ob/ob) from 4 independent experiments. (G) Quantitation of ER perimeter and (H) number of mitochondria. The morphometric analysis of the TEM pictures were calculated from average of 50 pictures (10 pictures per animal) in each experimental group (from 5 different animals per group). (I) 3D reconstruction of serial TEM sections obtained from independent samples taken at 11000x of single mitochondria, scale bar: 500nm. All the graphs represent mean ± SEM, *P < 0.05, Student's t-test.
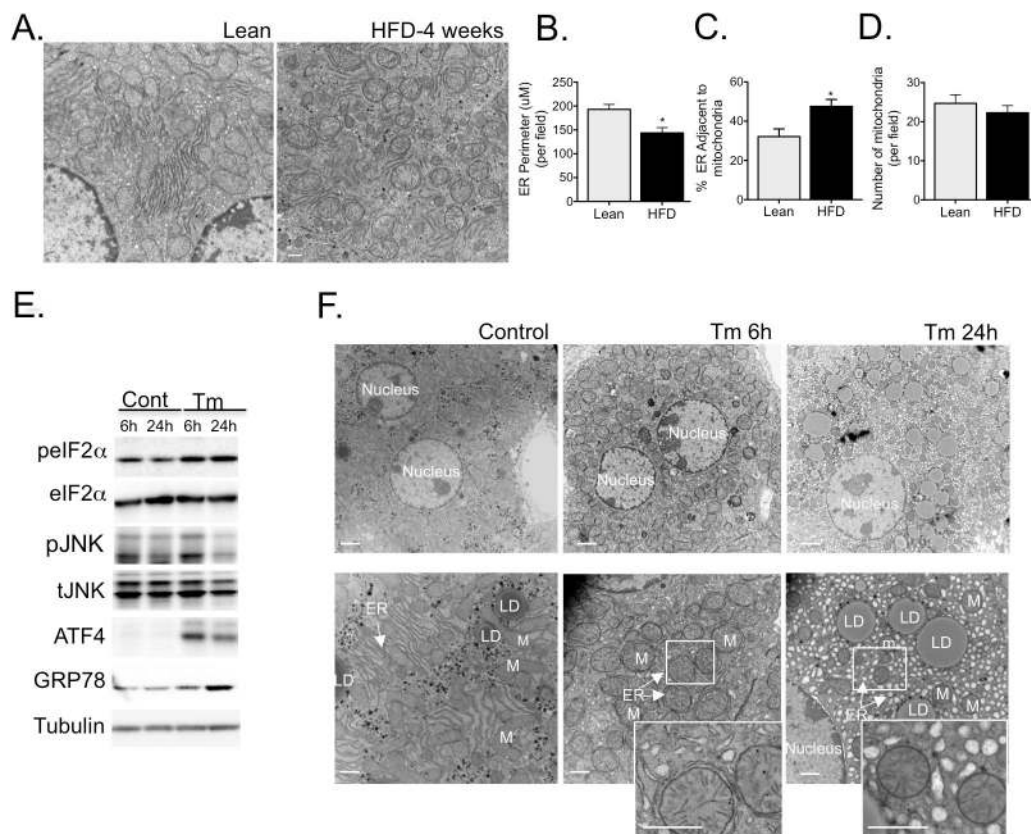
Figure 2. ER structural and functional changes in response to acute stress

(A) Representative TEMs of liver sections from wild type mice following 4 week challenge with regular chow or HFD. (B) Quantitation of ER perimeter (C) ER length adjacent to mitochondria normalized by total ER length (D) Number of mitochondria. The morphometric analysis were calculated from average of 18 pictures (~ 5 pictures per animal) in each experimental group (from 3 different animals per group) using Image J. (E) Evaluation of cell stress signaling activation in liver following 6 or 24 hours of tunicamycin (TM) exposure by western blot. (F) Representative TEMs of liver sections from wild type mice following 6 of 24 hours of TM treatment. Scale bar: 2um (upper panel) and 500nm (lower panel), n=3. The graphs represent mean ± SEM, *P < 0.05, Student's t-test.
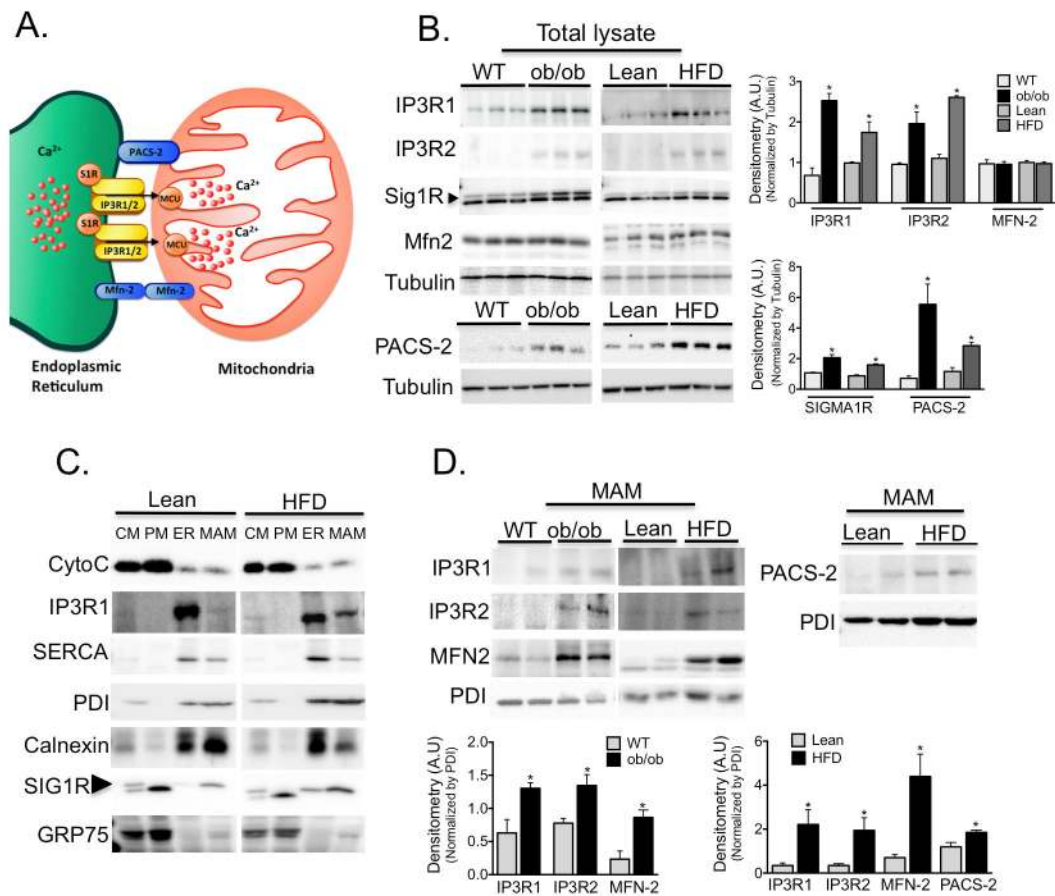
**Figure 3. Regulation of MAM enriched proteins in obesity**

(A) Schematic illustration of functional and structural MAM proteins. (B) Western blot and image J based quantification analysis of indicated proteins in liver total lysates from wt/*ob/ob* and lean/HFD-fed (16 weeks) mice. Arrow indicates the specific Sig1R band, n=3 representative of 2–3 independent experiments. (C) Western blot analysis of indicated proteins of subcellular fractions from mouse livers. CM: crude mitochondria. PM: Pure mitochondria, ER: endoplasmic reticulum and MAM: mitochondria associated ER membranes. Cytochrome C (Cyto C) was used as a mitochondrial marker; IP3R and SERCA were found mostly in the bulk ER. PDI and Calnexin were equally distributed between ER and MAM, and Sigma 1 receptor (Sig1R) enrichment served as a known MAM marker. This figure is representative of at least 5 different preparations (D) Western blot and quantification analysis of indicated proteins in MAMs from wt/*ob/ob* and lean/HFD mice, n=3. PDI served as a loading control. All the graphs represent mean ± SEM, *P < 0.05, Student's t-test.
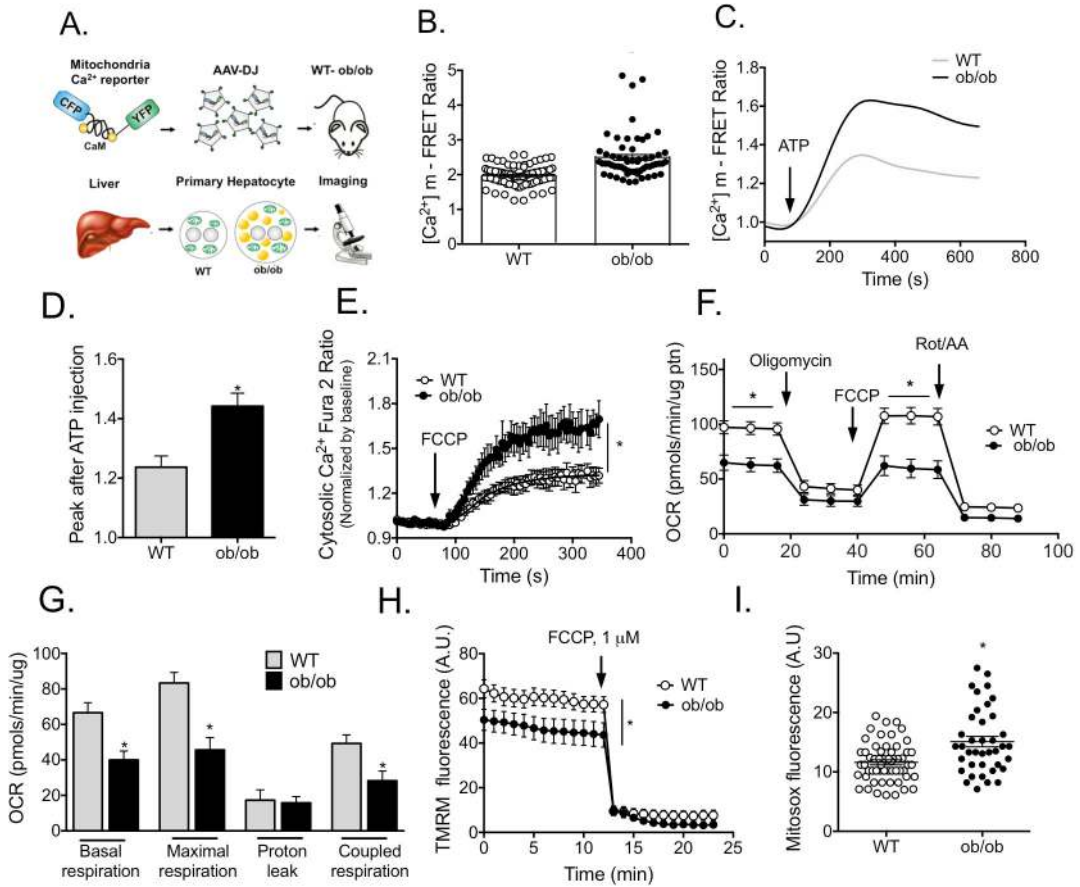
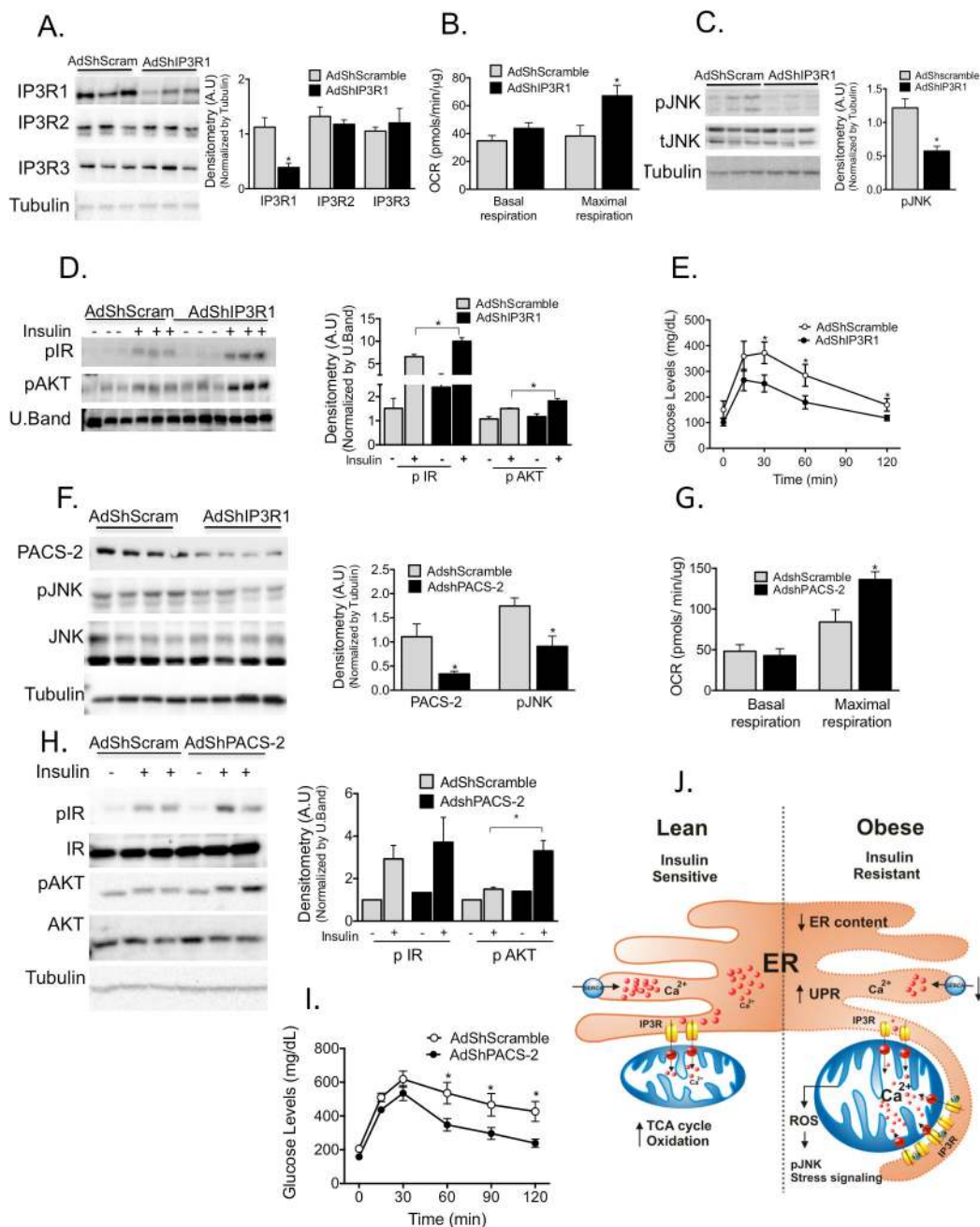**Figure 4. Obesity alters mitochondrial calcium flux liver**

(A) Schematic depicting the details of the experimental procedure used to measure mitochondrial Ca^{2+} levels in primary hepatocytes. (B) Mitochondrial Ca^{2+} content in primary hepatocytes from wt and *ob/ob* mice measured by FRET of 4mtD3cpv, n= 81 (wt) or 60 (*ob/ob*) cells, 4 independent experiments. (C) Representative trace of $[Ca^{2+}]_m$ upon 100uM ATP stimulation. (D) Quantification of the Ca^{2+} peak after ATP stimulation, n=15 cells, 4 independent experiments. (E) Cytosolic Ca^{2+} measured with 4μM of Fura 2-AM after 1μM FCCP treatment, n=60 (wt) or 40 (ob/ob) cells, 3 independent experiments. (F–G) Oxygen consumption rate (OCR) of primary hepatocytes from lean and *ob/ob* mice in basal assay medium (basal respiration), in the presence of 2μM olygomicin, (ATPsynthase inhibitor), 1μM FCCP (uncoupling agent) and 2μM Rotenone (Rot) and 2μM antimycin (AA) (complex I and III inhibitors, respectively). Maximal respiration, proton leak and coupled respiration were determined as described in methods section, n=11 (wt) n=13 (ob/ob) plates, 7 independent preparations. (H) Mitochondrial membrane potential in isolated hepatocytes from wild type and *ob/ob* mice, n=23 (Wt), n=15 (ob/ob), representative of 3 independent experiments (I) ROS production measured with 3μM mitosox loading. n=57 (wt) and 39 (*ob/ob*) cells from 3 independent experiments. All the graphs represent mean ± SEM, *P < 0.05, Student's t-test.
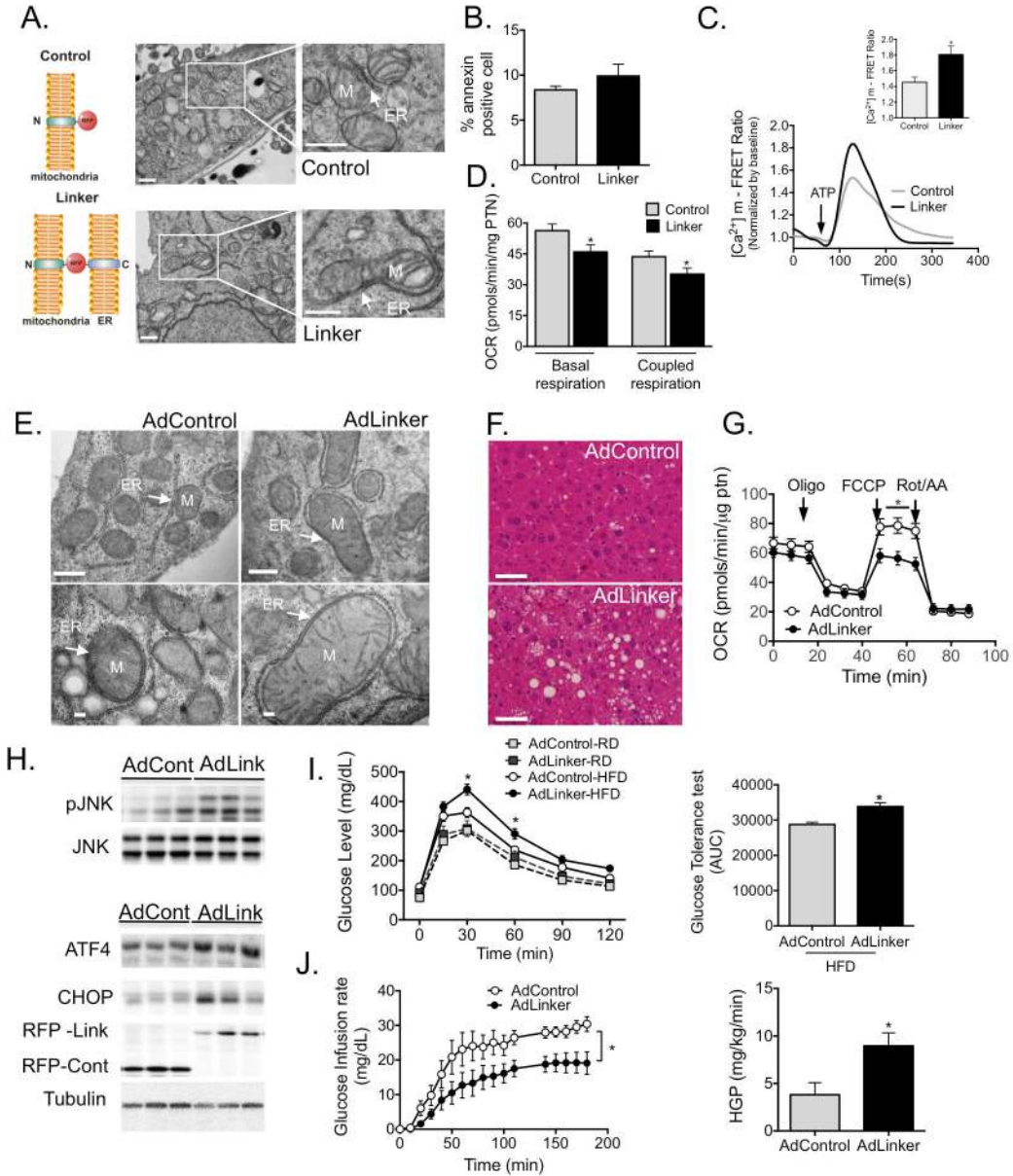
Figure 5. Experimental induction ER-mitochondria interactions increases mitochondrial calcium flux and impairs glucose homeostasis

(A) Schematic illustrating the mitochondrial-ER synthetic linker. The construct encodes a monomeric red fluorescent protein (RFP) fused to the OMM targeting sequence of mAKAP1 at the N terminus and the ER targeting sequence of yUBC6 at the C terminus with a length of ≈25 nm[25]. Representative TEM of Hepa 1-6 cells expressing control (upper panel) and linker plasmids (bottom panel) at 9300x, scale bar: 500nm. (B) FACS analysis of Annexin V positivity in control and linker-expressing cells, n=3. (C) Representative trace of mitochondrial Ca^{2+} dynamics in single Hepa 1-6 cells expressing the control or linker construct, measured by FRET of 4mtD3cpv following treatment with ATP (100μM). (C inset) Quantification of the peak in Ca^{2+} after ATP stimulation, 3 independent experiments. (D) Measurement of oxygen consumption rate (OCR) in control and linker-expressing Hepa

1-6 cells in the presence of 2μM Oligomycin, 0.4 μM FCCP and 2μM Rotenone (Rot) and 2μM antimycin (AA). n=15 from 4 independent experiments. (E) Representative TEMs of liver sections from lean mice expressing the control or linker construct, scale bar: 500nm upper panel and 100nm bottom panel (F) Liver sections from HFD-fed mice expressing control or linker constructs, stained with hematoxylin and eosin, scale bar 50um. (G) OCR of primary hepatocytes from HFD-fed mice expressing control or linker constructs, n =10, from 3 independent preparations. (H) Western blot and quantification analysis of indicated proteins in liver lysates from HFD-fed mice expressing control or linker constructs. (I) Glucose tolerance test (GTT) and area under the curve of mice expressing control or linker constructs, n=6 (Ad control-RD, Adlinker-RD and Adcontrol-HFD) n=7 (Adlinker-HFD). (J) Glucose infusion rate and Hepatic glucose production during hyperinsulinemic-euglycemic clamp in HFD-fed mice expressing control or linker constructs, n= 8 for Adcontrol and 11 for Adlinkers. All data are mean +/− SEM, *P <0.05 (two-way ANOVA for panel M or Student's t-test for the others).

Figure 6. Experimental suppression of MAM function or formation alters mitochondrial calcium flux and improves glucose homeostasis
(A) Western blot and quantification analysis demonstrating specific knockdown of IP3R1 in liver lysates following adenoviral shRNA transduction, n= 3, representative of 2 independent experiments. (B) Oxygen consumption rate of primary hepatocytes from mice expressing control or shIP3R1, n=6. (C) Western blot and quantification analysis showing reduced JNK phosphorylation in liver lysates following IP3R1 knockdown. (D) Western blot and quantification analysis of the insulin-action in the liver samples following expression of shScramble or shIP3R1. n=3. (E) Glucose tolerance test in mice expressing

shScramble or shIP3R1, n=7. (F) Western blot and quantification analysis demonstrating specific knockdown of PACS-2 in liver lysates following adenoviral shRNA transduction, n=4 representative of 2 independent experiments. (G) Oxygen consumption rate of primary hepatocytes from mice expressing control or shPACS-2, n=5 for shscramble and n=8 for shPACS-2. (H) Western blot and quantification analysis of the insulin-action in the liver samples following expression of shScramble or shPACS-2, n=3. (I) Glucose tolerance test in mice expressing shScramble or shPACS-2, n=7 for shScramble and 9 for shPACS-2. (J) We propose here that an early development in the course of obesity-induced metabolic disease is increased MAM formation in the liver. Increased MAM formation drives higher calcium transfer from ER (via IP3R1) to the mitochondria, leading to calcium overload, which in turn leads to impairment in mitochondrial oxidative capacity, increased ROS generation, cellular stress, impaired insulin action in the liver and abnormal glucose metabolism. All data are mean +/− SEM, *P <0.05, Student's t-test for the others.